Untethered Robotic Millipede Driven by Low-Pressure Microfluidic Actuators for Multi-Terrain Exploration

Qi Shao, Xuguang Dong, Zhonghan Lin, Chao Tang, Hao Sun, Xin-Jun Liu, and Huichan Zhao, *Member, IEEE*

***Abstract*—Mobile robots that can adapt to an extensive range of terrains play essential roles in many applications. Millipedes are one of the most terrain-adaptive creatures in nature due to their multi-legged locomotion and flexible body. Inspired by natural millipedes, we report an untethered robotic millipede with a 6-segments soft-rigid hybrid body that can actively bend and 24 legs driven by low-pressure microfluidic actuators. The 24 microfluidic actuators are driven by two independent low-pressure sources from miniature pumps, which allows the untethered locomotion of the robotic millipede in small size (length, 23 cm; width, 5 cm; height, 4 cm) and lightweight (150 g). Using a pre-defined gait for the multi-legs, the robotic millipede can locomote with a maximum speed of 30.96 cm/min (1.35 body length per minute) and a minimum turning radius of 15 cm (0.65 body length). Experiments also demonstrated that the robot was able to locomote effectively in various uneven terrains. Utilizing its passive or active mode of its flexible body, the robot could also achieve adaptive moves. The robotic millipede has the potential to perform a variety of environment exploration tasks by remotely controlling and transmitting real-time images wirelessly.**

***Index Terms*—Soft robot materials and design, biologically-inspired robots, soft robot applications.**

I. Introduction

IN MANY application scenarios like search and rescue after the earthquake, underground archaeology, and topographic survey, small and agile autonomous mobile robots that can adapt to a large range of terrains can play a big role [1]. Existing ground mobile robots can be divided into two categories: engineered type (e.g., wheeled and tracked robots) [2] and bioinspired type (e.g., bipedal robot, quadrupedal robot, snake robot, inchworm robot, earthworm robot, etc.) [3], [4], [5], [6], [7], [8]. Bioinspired mobile robots exhibit higher adaptivity to unstructured environments because these robots are inspired by the long-term evolved features of creatures, such as high-power muscles [9], legs [10], soft-rigid hybrid bodies [11], and other smart mechanisms [12].

Among all types of creatures, millipedes–one of the first-ever terrestrial animals on earth [13], have been existing for 400 million years and are widely distributed on all continents of the earth except the Antarctica [14]. Their high adaptivity to complex terrains, large payload-to-weight ratio [15], and morphological robustness from tens or even hundreds of legs, have motivated many multi-legged robots in the past 30 years. Earlier versions of multi-legged robots usually had legs and backbone bodies designed as serial links driven by many motors, and the dimensions were usually above 1 m [16], [17]. Later, many efforts have been put into employing passively flexible body and flexible legs [18], [19] to further increase their capability to adapt to uneven terrains. Active actuation of the backbone body [20], [21] has demonstrated higher maneuverability and obstacle-crossing capability. Though very impressive, the above-mentioned work utilizes motors to achieve both the leg and body motions. Thus, they are usually large and heavy, which may limit their capability in small-space exploration.

Alternatively, new smart materials have been utilized to construct much smaller multi-legged robots. Scientists have developed insect-scale multi-legged robots actuated by piezoelectric bimorph actuators and investigated how leg failures affect the robot's performance [22], [23]. Though these microrobots achieved impressive locomotion, the high-voltage driving power supplies and the fragility of piezoelectric actuators may inhibit their practical applications in the wild. Multi-legged soft millirobot with its body material filled with magnetic particles can be actuated in a magnetic field and achieve extraordinarily multimodal locomotion [24], [25], [26], [27], yet these types of robots need external apparatus to generate the magnetic field, limiting its application for field exploration [24]. Microfluidic actuators can deform with fluidic pressure and have facilitated small-scale soft robots with complex motions (grasping, quadrupedal walking, octopus-inspired motions, etc.) [28], [29], [30], [31], [32], [33]. In addition, microfluidics can be easily manufactured (i.e., by soft lithography) into actuator arrays powered by a single fluidic source with no complex transmissions [34]. Their inherent compliance can naturally maintain the structure's flexibility and high toughness [35]. Therefore, a multi-legged robot constructed from soft microfluidic actuators has the potential to demonstrate more robust and agile mobility in harsh environments. However,

Manuscript received 16 June 2022; accepted 26 September 2022. Date of publication 10 October 2022; date of current version 14 October 2022. This letter was recommended for publication by Associate Editor P. Chirarattananon and Editor Y.-L. Park upon evaluation of the reviewers' comments. This work was supported in part by the National Key R&D Program of China under Grant 2019YFC1520100, and in part by the National Natural Science Foundation of China under Grants 51975306, 92048302, 52222502, and 52105028. *(Corresponding author: Huichan Zhao.)*

The authors are with the Department of Mechanical Engineering, State Key Laboratory of Tribology in Advanced Equipment, and Beijing Key Lab of Precision/Ultra-Precision Manufacturing Equipment and Control, Tsinghua University, Beijing 100084, China (e-mail: sq19@mails.tsinghua.edu.cn; dxg19@mails.tsinghua.edu.cn; linzh19@mails.tsinghua.edu.cn; wstcsues@163.com; haos@mail.tsinghua.edu.cn; xinjunliu@mail.tsinghua.edu.cn; zhaohuichan@mail.tsinghua.edu.cn).

This letter has supplementary downloadable material available at https://doi.org/10.1109/LRA.2022.3213137, provided by the authors.

Digital Object Identifier 10.1109/LRA.2022.3213137

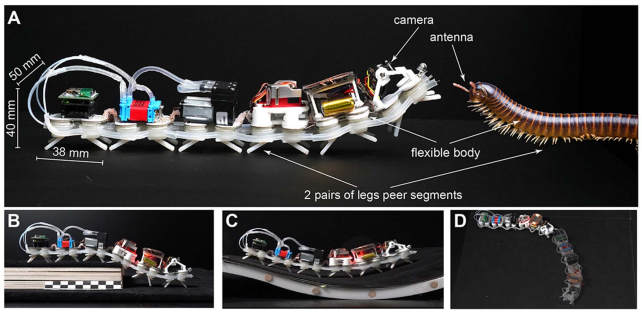

Fig. 1. Appearance and motions of the proposed robotic millipede. (a) Photograph of the proposed robotic millipede and its comparison with a natural millipede (dimensions are not in its actual scale, and the milipede picture is modified from a third party image by Thomas Shahan: www.flickr.com/photos/49580580@N02/15241792676/). Photographs of the robot in the process of (b) climbing up an obstacle, (c) walking on an undulating surface, and (d) steering.

challenges such as designing the body and leg morphology, fabricating actuators with sufficient payload and range of motion, and developing an appropriate type of gait to facilitate effective locomotion still need to be addressed [15], [36].

In this work, inspired by several key features of natural millipede, we report an untethered robotic millipede with a soft-rigid hybrid body that can actively bend and a number of legs driven by low-pressure microfluidic actuators (Fig. 1). Specifically, the robot has 6 segments and 24 legs (half of these legs are flexible legs). The robot is of small size (length, 23 cm; width, 5 cm; height, 4 cm) and lightweight (150 g), with all necessary driving, control, and communication units onboard (pumps, valves, battery, motors, controllers, camera, and image transmission module). We first report the design, fabrication, and analysis of all robot components. Then, a type of gait for achieving forward and backward locomotion that requires only two independent pressure sources is developed, and the hybrid body's active bending facilitates the robot to turn and head up. Next, in the experimental section, we tested the robotic millipede in the lab. We got a maximum translational speed of 30.96 cm per minute at a driving frequency of 0.83 Hz and the minimum turning radius is 15 cm on flat and smooth surfaces, and was able to cross terrain with drop up to 3 cm. Finally, we demonstrate its potential for field exploration by remotely controlling the robot to locomote on uneven terrain and collecting its real-time images.

II. Design and Manufacturing of the Robotic Millipede

A. Overall design

We first describe the overall design of our bioinspired robotic millipede. Similar to a natural millipede, our robot has a flexible backbone and multiple legs (Fig. 1(a)). The robot's backbone comprises 6 rigid segments connected by 5 flexible joints. The first two flexible joints can actively bend horizontally and vertically driven by fiber tendons. The robot has in total 24 legs distributed evenly on the 6 segments, and each leg is actuated by microfluidic actuators directly cast onto the backbone. These 24 actuators are divided into two groups with each group of actuators connected by internal microchannels. Half of the 24 legs located in front are one-direction flexible legs that can bend over when blocked by obstacles, and the other half of the legs are

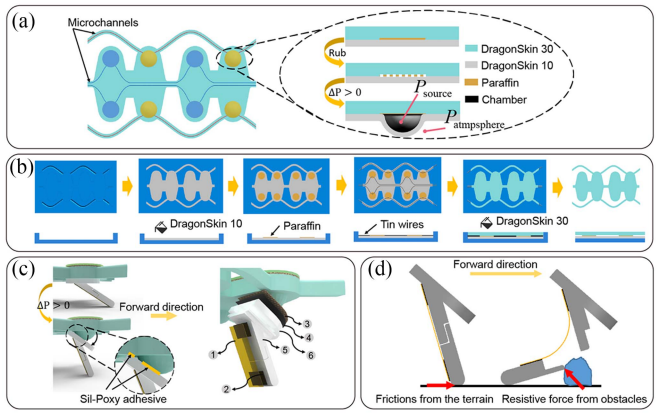

Fig. 2. Design and fabrication of the microfluidic actuator array and the flexible legs. (a) Diagrams showing the actuation principle of a microfluidic actuator and the connecting channels between actuators. (b) Fabrication steps of the microfluidic actuator array consisting of 8 individual chambers. (c) Diagrams showing the connection between a microfluidic actuator and a flexible leg and the actuation principle of the leg's swing motion (the flexible leg including: 1-a piece of 0.3mm-thick polyimide film; 2-a piece of carbon fiber plate; 3-a piece of fabric cloth; 4-a piece of VHB tape (3 M); 5-detachable leg; 6-leg base (d) The working principle of the flexible leg upon contact force from different directions.

rigid ones. Thanks to the flexibility of its backbone, actuator, and legs, this untethered multi-legged robot successfully achieved forward motion in some usual terrains, such as with obstacles (Fig. 1(b)) and curved surfaces (Fig. 1(c)) and steering motion when needed (Fig. 1(d)).

B. Microfluidic Actuators and Flexible Legs for Achieving Multi-Legged Motions

The entire robotic millipede has 24 legs actuated by 24 microfluid chambers. Each microfluidic chamber's motion is driven by the pressure difference between the pressure of the drive source and atmospheric pressure, as shown in Fig. 2(a). To reduce the number of pressure sources, we would like to actuate multiple actuators simultaneously using a single pressure source. We designed micro-channels connecting the individual chambers and divided the 24 chambers into two groups so that only two independent sources are required. The robotic millipede consists of 3 identical actuator array units with 8 chambers each as shown in Fig. 2(a). This modular design can improve the robot's expansion capability and reduce fabrication's complexity. In Fig. 2(b), we describe the fabrication method of the actuator array unit with 8 chambers. First, a mold with the designed shape was 3D printed. Next, we poured silicon pre-elastomer (DragonSkin 10 slow, Smooth-On) evenly into the mold to form a uniform membrane with the designed thickness. Then after first membrane got cured, we placed 8 round paraffin slices on top of the membrane in designed position, which later formed the internal chambers of the actuators. In the next step, we put tin wires onto the paraffin slices, which would later form the connecting microchannel between chambers. Finally, we poured another stiffer silicone pre-elastomer (DragonSkin 30, Smooth-On) to fill the entire mold. After curing, we removed the final product from the mode and took out the tin wires. The paraffin slices were left in the cured piece and they were rubbed into tiny fragments. When the compressed air was fed into the channels through the micro-channels, the layer made of DragonSkin 10 expanded outward as expected (see Fig. 2 (a)). It

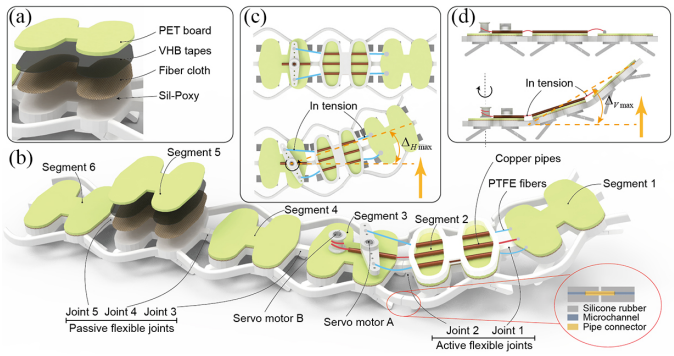

Fig. 3. Structure and actuation of the soft-rigid flexible body of the robotic millipede. (a) The stiffness-enhanced structure of a body segment. (b) The overall design of the soft-rigid flexible body and its mechanical and pneumatic connections. (The inset image shows the cross sectional diagram of the pneumatic connection of micro-channels.) (c) Bending in the horizontal direction using two tendons. (d) Bending in the vertical direction using one tendon.

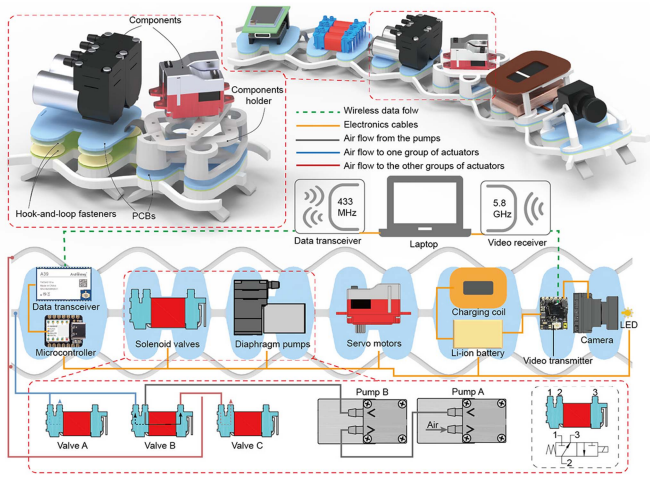

Fig. 4. Distribution and connection of components on the robot.

is worth noting that the above fabrication method is also suitable for making actuator arrays with different shapes, arrangements, and actuator diameters as small as 2 mm, for robots used in more scenarios.

To convert the expansion deformation of the chambers into a swing motion of a robotic leg, we glued the legs to the outer layer of the chambers using adhesive (Sil-Poxy, smooth-on), as shown in Fig. 2(c). Due to the low adhesive strength between silicone rubber and the 3D printed plastics, we also added two other layers in between to enhance the adhesion, including a piece of fabric cloth and a piece of VHB tape. After adhesion, the leg would swing once the chamber expands out. The swing center is roughly at the end point of the leg's connecting base. The leg is also designed with a detachable base to facilitate fast replaceability of different types of legs. We design two types of legs. One type is simply a rigid piece that is oriented at an inclined angle with the leg base. The other is a flexible leg. The flexible leg is designed to have uni-directional flexibility to improve the robot's obstacle surmounting capability. The flexible leg has a elastic flexible hinge made of polyimide film, as shown in Fig. 2(c). This flexible leg can support the forward friction and stay straight and rigid in standard cases. Yet when obstacles hinder the leg, the flexible leg will bend as shown in Fig. 2(d), to overcome obstacles. This flexible leg can improve the passing ability of the robot on rough terrains. Due to that the legs pointing forward are prone to be stuck with obstacles, in each body segment, the two front legs are designed as flexible legs, and the two rear legs are rigid legs. So the robot has in total 12 flexible legs and 12 rigid legs.

C. Design and Actuation of the Soft-Rigid Flexible body

By connecting the microchannels between the three microfluidic actuator array units through pipe connectors, an array with 24 chambers can be constructed. As shown in Fig. 3(a), PET plates are used to enhance the stiffness of each segment to increase the load capacity of each segment. As a result, the robotic millipede gets a soft-rigid hybrid body consisting of 6 rigid segments and 5 flexible joints connecting them (Fig. 3(b)). Three PTFE fibers are used as tendons to actively bend the body, with one end of each fiber fixed on segment 1. Passing through copper pips on segment 2 and segment 3, the three tendons are driven by 2 servo motors placed on segment 3 as shown in Fig. 3(b). Therefore, the motors and tendons can control the active bending of joint 1 and joint 2, whereas joints 3-5 remain passively flexible. Fig. 3(c) shows servo motor A drives the two tendons to control the horizontal bending of joint 1 and joint 2. Servo motor A can rotate within a range of -60 degrees to 60 degrees relative to the initial position. When it turns to one side, the tendon on the turning side gets in tension while the other tendon releases, allowing active, horizontal bending with a 30° maximum angle of one-side bending ($\Delta_{H\max} = 30°$). Fig. 3(d) shows how the middle tendon driven by servo motor B controls joint 1 and joint 2 to bend up and down with a 25° maximum angle of head up ($\Delta_{V\max} = 25°$).

D. Electronic Components Integration for Untethered Locomotion

To achieve the robot's untethered locomotion and add additional functions such as remote control and data collection, we equipped the robot with all necessary components on itself as shown in Fig. 4. The components are distributed on the segments fixed by the mechanical holders or directly on the printed circuit boards (PCBs). The PCBs have the same shape as the rigid area of each segment. The PCBs are connected by flexible cables, which can transmit information and power with negligible effect on the flexibility of the joints. Meanwhile, the PCBs and the body of the robotic millipede are connected by hook-and-loop fasteners that can be quickly installed and disassembled for replacement or reconstruction. The equipped components include: 1) an image acquisition system composed of an LED, a camera (Pico 1200tvl, FOXEER), and a video transmitter (Unify pro32 nano, TBS), used to collect images and transmit them back to the host computer wirelessly for navigation and control in real-time; 2) an energy supply system consisted of a lithium battery (350 mAh, TATTU) and a charging coil, supplying the energy required for the entire robot; 3) the active bending driving components for the body composed of two servo motors; 4) the pneumatic driving components composed of three miniature pneumatic solenoid valves (X205LF, Parker) and two micro diaphragm pumps (T2-05IC, Parker) with one-way flow; and 5) the control component composed of data transceiver and

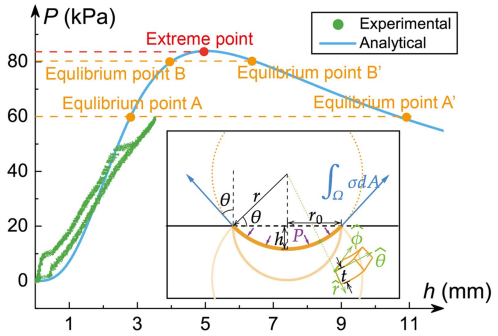

Fig. 5. Modeling and experimental results of a single chamber's motion with pressure. (Inset image: simplified force diagram of a single chamber under pressure).

microcontroller, used to transmit commands and data from and to the host computer.

Pneumatic components are connected by silicone rubber hoses. Pump A and pump B are connected in series, i.e., the inlet of pump A is connected to the atmosphere to let air in, and the outlet of pump A is connected to the inlet of pump B. This serial connection can amplify the output pressure and flow. The three 2-positon 3-way universal solenoids control the flow from the serial pumps. Valve B is a switch valve that can select the airflow to connect to which groups of chambers. Due to the reverse cut-off feature of the pump, the independent actuation and holding of the two groups of chambers are achieved by controlling the pumps and valve B. Valves A and C are bleed valves; thus, when emerging, the chambers will be connected to the atmosphere to deflation. The electronic connections, data flow, and air flows are shown in Fig. 4 with lines in different colors. The total weight of the robot with all components is 150 g.

III. Modeling and Analysis of the Actuator and the Robot

A. Modeling of the Microfluidic Actuator

The relationship between the driving pressure and the height of each chamber is a crucial characteristic of each leg's swing motion. To understand this relationship, we established a static model of the actuator's motion under pressure. As shown in the inset diagram of Fig. 5, when the pressure difference between the inside and outside of the chamber is zero ($P_0 = 0$), the chamber is flat, and we define this state as the initial state. The shear modulus of the material of the membrane is μ, and the radius and thickness of the membrane in the initial state r_0 and t_0, respectively. When the pressure difference P is greater than 0 ($P_0 > 0$), the chamber's membrane bulges outward as a spherical cap [37]. At this state, the radius of the actuator is r and the thickness is t. Under the quasi-static pressure of P, a spherical coordinate system is established with the center of the membrane as the origin. From the symmetry of the structure, we know that σ_θ is equal to σ_ϕ, and we denote it as σ. We use the neo-Hookean model as the constitutive model for the membrane and assume it is an incompressible hyperelastic material. Thus, we get the following relationship between the stress and the stretch:

$$\sigma = 2\mu\left(\lambda_\theta^2 - \frac{1}{\lambda_\theta^4}\right) \tag{1}$$

where λ_θ is the principal stretch in the $\hat{\theta}$ direction and μ is the material's shear modulus. Since the force of the chamber's deformation is axially symmetric, its force balance equation in the vertical direction is written as:

$$P\pi r_0^2 = \sigma \cdot 2\pi r_0 t \cdot \cos\theta \tag{2}$$

where θ is the angle between the stress in plane and the vertical direction. From the geometric relationship, we have $\cos\theta = r_0/r$. From the material's incompressibility assumption and geometric symmetry, we have:

$$\lambda_\theta^2 = \lambda_\phi^2 = \frac{1}{\lambda_\mathrm{r}} = \frac{t_0}{t} \tag{3}$$

where $\lambda_\phi, \lambda_\mathrm{r}$ is the principal stretch in the $\hat{\phi}, \hat{r}$ direction. As shown in the Fig. 5, we take the height of the spherical crown as h, and from the geometric relationship, we can get

$$\sqrt{r^2 - r_0^2} = |r - h|. \tag{4}$$

Thus,

$$\lambda_\theta^2 = \frac{S}{S_0} = \frac{2\pi r h}{\pi {r_0}^2} = \frac{h^2 + r_0^2}{{r_0}^2}. \tag{5}$$

Substitute (1) and (3)–(5) in to (2), we get

$$P = \frac{4\,h^3 t_0 \mu\left(h^4 + 3\,h^2 r_0^2 + 3 r_0^4\right)}{\left(h^2 + r_0^2\right)^4}. \tag{6}$$

Substitute in the material properties and geometric dimensions $\mu = 114300$ Pa [38], $r_0 = 4$ mm, $t_0 = 1.6$ mm, we get the plots in Fig. 5. From the plot in Fig. 5, we see that when the applied pressure is below the extreme point, the membrane has two equilibrium states: one with a small height and the other with a large height. In practical uses, the deformation of the membrane may switch between the two states due to external disturbances. Therefore, when multiple actuators are connected and actuated simultaneously, they may exhibit different heights. As seen from the curves in Fig. 5, the closer the applied pressure is to the extreme point, the more effortless such switch between the two states (B and B') is to occur with external perturbations, since the actuator volumes in the two states are similar. Therefore, to avoid such a switch of states, we have set our applied pressure well below the extreme point, so the actuators stay at the first equilibrium point and don't switch to the other easily. The final goal is that all actuators stay at the first equilibrium point (e.g., equilibrium point A in Fig. 5) at the same pressure. Based on the above rationale, we chose 60 kPa as the applied pressure. The dotted green line in the plot shows our experimental results of the chamber's deformation at varying pressures.

B. Motion Analysis of the Robotic Millipede's Plane Forward Motion

The entire robot consists of three identical actuator array units connected in series and 24 chambers and legs. Each leg can swing at an angle of θ driven by its chamber as shown in Fig. 6(a). The minimal unit of these chambers consists of two chambers–the forward one with the leg pointing forward and the back one with a leg pointing backward. Fig. 6(b) shows our designed gait with only two pairs of legs shown. The other legs are operating in the same manner. A full cycle of the gait is divided into four phases (A, B, C, D), and we name the forward leg in each leg pair as "leg A" and the backward leg as "leg B". In each phase, only one leg

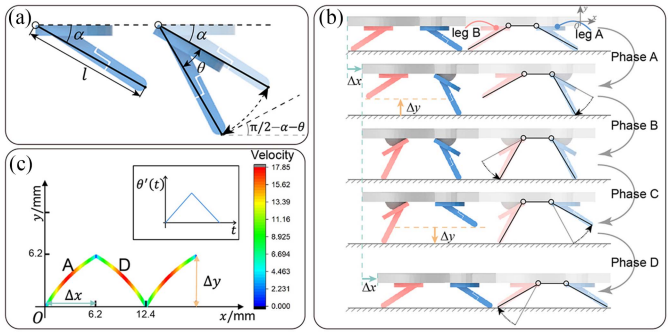

Fig. 6. Gait and kinematic analysis of robotic millipede's forward locomotion. (a) Design parameters of a swing leg. (b) Designed gait and movement sequences of two pairs of legs of a complete cycle. (c) Motion trajectory and velocity of the robot's center of mass of the designed gait.

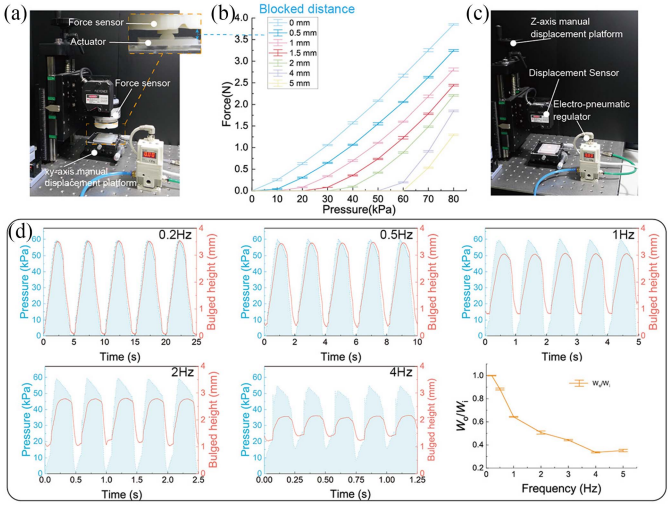

Fig. 7. Static and dynamic performance of the microfluidic actuator. (a) Experimental setup for static tests of the chamber's motion and force. (b) Test results of the chamber's blocked force with applied pressure for different blocked distances. (c) Experimental setup for dynamic tests. (d) Chamber's motion is driven by 0.2 Hz to 4 Hz input pressure.

moves – leg A moves in phase A and C, and leg B moves in phase B and D. This gait makes it possible to use one switch valve to drive two groups of actuators. In phase A, the clockwise rotation of leg A about its leg tip pushes the robot to move forward for $\Delta x = l\cos\alpha - l\cos(\alpha+\theta)$ in the horizontal direction, where l is the length from the leg tip to the center of rotation, and α is the leg's initial inclined angle with the horizontal direction, and θ is the rotational angle under pressure. Meanwhile, the center of mass of the robot moves $\Delta y = l\sin(\alpha+\theta) - l\sin\alpha$ in the vertical direction. During phase B, leg B is actuated and rotates at an angle of θ counterclockwise. In phase C, leg A is de-actuated and rotates back to its initial position, and at the same time, the support leg switches from leg A to leg B. In other words, by the end of phase C, the tip of leg B is in contact with the ground. In phases B and C, the robot's center of mass stays unmoved. In phase D, leg B is de-actuated and it rotates back to its initial position about its tip, pushing the robot to move forward in the horizontal direction and upward in the vertical direction. The distance in the horizontal and vertical directions is the same as in phase A. The total distance of the robot's center of mass moves forward in one period is $2\Delta x$, and we call it a step distance. We could easily find that longer legs would result in a larger step distance. However, in real cases we have to make sure the legs are not interrupting each other; therefore, we have a leg length limit for our leg design. α is a key parameter that determines the step distance and the step height change. We have chosen an α to achieve similar Δx and Δy so that the robot can overcome a certain height and maintain a big step distance. We substitute the dimensions of our constructed robot ($l = 17$ mm, $\theta = \pi/6$, and $\alpha = \pi/6$), for the above gait, the trajectory of the robot's center of mass in a completed cycle is drawn in Fig. 6(c), which consists of two pieces of arcs. If θ accelerates first and then immediately decelerate both at constant acceleration rates in phase A and D, we could also draw the robot's velocity over the trajectory. The color bar in Fig. 6(c) indicates the robot's velocity along the trajectory when each phase lasts 1 s. From the structure of the robotic millipede, we can see that if leg A and leg B are rigid legs, the whole robot will be symmetric from front to back, and thus the backward and forward movements are exactly equivalent. However, if half of the legs are designed as flexible legs, the robot will not be able to achieve the backward movement, because the flexible legs facing backward cannot bear the moment from forces from the forward directions.

IV. Characterization of the Microfluidic Actuator, Module, and the Robot

A. Characterization of the Microfluidic Actuator's Static and Dynamic Performance

In this section, we characterized the static and dynamic of a single chamber composed of the microfluidic actuator array to drive the robot's 24 legs. The chamber deformation was converted into force and displacement to perform external work. To evaluate the chamber's capacity, as shown in Fig. 7(a), we used a force sensor (KWR75 A, Kunwei) and tested its blocked force with pressure at different blocked distances. The blocked distance was the distance between the force sensor and the chamber when no pressure was applied. The input pressure gradually and discretely increased from 0 to 60 kPa, which was the optimal working range of the chambers when there was no blocking, as discussed in Section 3.1. The experimental results are shown in Fig. 7(b). It indicates that a single chamber can generate a fully-blocked force of up to 2.8 N (i.e., the blocked distance was zero) at 60 kPa. When the blocked distance increased to 5 cm, the blocked force was almost zero at 60 kPa.

The dynamic performance of the chambers is essential for us to drive the robotic millipede to move rapidly. To characterize its dynamic performance (Supplementary Video Part 1), we established an experimental setup as shown in Fig. 7(c) to test the chamber's bulging height at different pressures and frequencies. As Fig. 7 (c) illustrates, a 700 kPa air cylinder and an electro-pneumatic regulator (ITV2010-312 L, SMC) were used to generate a sinusoidal pressure as the input pressure, and the chamber was fixed on the ground. We used a laser displacement sensor (LK-H050, Keyence) to measure its bulged height. Seven different frequencies from 0.2 Hz to 5 Hz with the same amplitude of 0 to 6 V were used as the input signal of the regulator. Limited by the dynamic performance of the regulator, the actual pressure applied to the chamber, and its bulged height at 0.2 Hz, 0.5 Hz, 1 Hz, 2 Hz, and 4 Hz are shown in Fig. 7(d). We also plotted the normalized ratios of the amplitude of the

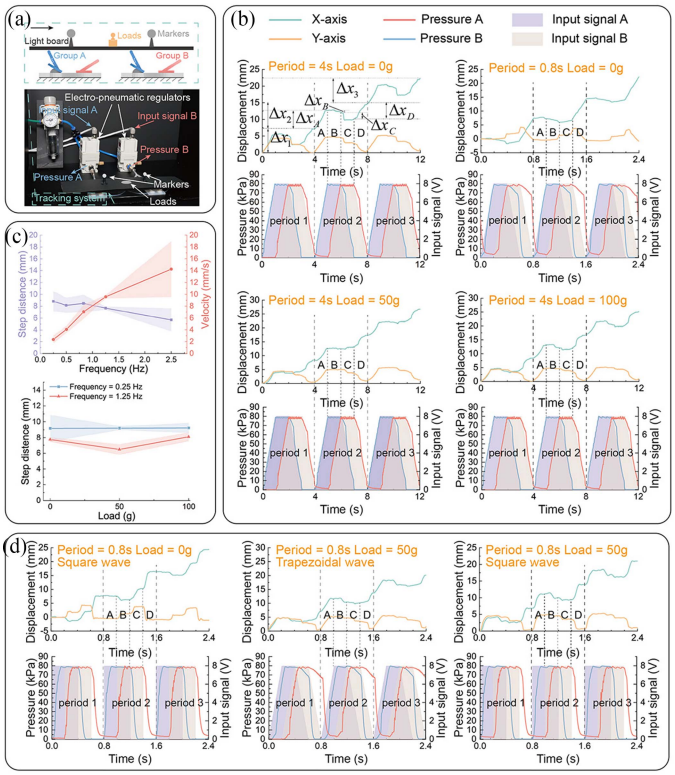

Fig. 8. Motion tests of two inverted units of the two-pair-leg units. (a) Experimental setup of the inverted units with boards on top of them. (b) The board's trajectories in the horizontal and vertical direction over time under different driving frequencies and loads. (c) Step distance and average velocity of the board with driving frequency and step distance with a load. (d) The board's trajectories in the horizontal and vertical direction over time with different load and driving signal waveforms.

bulged height to that of the input pressure (W_o/W_i) at different frequencies. As the results indicate, with the increase of the driving frequency, the W_o/W_i decreased gradually, and when the frequency exceeded 2 Hz, the W_o/W_i decreased below 0.5, which greatly affected the output motion of the leg. For the above reason, we preferably set the driving frequency to be within 2 Hz. Even if we use a better pressure source with no dynamic damping, the chamber's dynamic response should be considered and appropriately compensated in fast-driving mode.

B. Motion Tests of Inverted Actuator Array Units

To characterize the performance of the robotic gait proposed in Section III.B in actual locomotion, we inverted and fixed two units of the two-pair-leg units on the table and put a lightweight rigid board made of foam (5 g) on top of it, as shown in Fig. 8(a) (Supplementary Video Part 2), we have inverted the body-leg units so that we could investigate how the weight on the leg affected the robot's motions. These two units formed the smallest unit to achieve forward motions using the proposed gait without falling over. We fixed two markers on the light board to track its motion in space with a tracking system (V120: Trio, OptiTrack). When actuating the two groups of actuators following designed sequences to achieve the proposed gait, the light board moved forward due to the movement of the legs and frictions between the legs and the board. The board's motion indicates the robot's motion if the whole system is inverted back. The two groups of microfluidic actuators were driven by two electro-pneumatic regulators and using which we controlled the input pressure as shown in the photograph in Fig. 8(a). Different weights were placed onto the center of the board to investigate its motions under different loads.

We first investigated how the driving frequency and external load affected the board's motion. In Fig. 8(b), we show the board's horizontal and vertical motions over time in three cycles at four combinations of driving frequencies and external loads. The driving signals to the two regulators are drawn as shadows in the lower subplot of each sub-figure. The pressures of all A-legs were expected to rise linearly in phase A, stay constant in phase B, drop linearly in phase C, and stay at zero in phase D. The pressures of all B-legs were a phase later than that of B-legs. The total duration of four phases is called a period. At low driving frequencies, such as a period lasting four seconds, the pressure follows the driving signal to the regulators perfectly. In contrast, the pressure deviated from the driving signals at high driving frequencies, such as a period lasting only 0.8 seconds. As expected, the board went up and down in its vertical direction and moved forward in its horizontal direction in all cases (see upper subplot of each subfigure in Fig. 8(b)).

In the first subfigure with Period $= 4$ s and Load $= 0$ g, we divided the horizontal movement in a cycle according to the phases. As analyzed in previous sections, and is expected to be zero and is expected to be equal and greater than zero. In experimental results, we can see that and were less than 0, which meant the board was moving backward in phases B and C. As the load and driving frequency increased, these backward motions were reduced, yet the forward motions also decreased. As a final result, as shown in Fig. 8(c), the step distance decreased with driving frequency, but the overall forward velocity increased. The step distance stayed almost constant with external loads up to 100 g. This data indicates that our robot can hold up to 300 g of loads without noticeable deterioration in its moving speed.

Finally, we investigated the effect of the driving signal's waveform on the board's motions. We could see from Fig. 8(d) that when a square wave was used rather than a trapezoidal wave, the backward motions in phases B and C were more pronounced, thus causing the board's forward velocity to be lower. In addition, the forward speed with the trapezoidal wave is more stable.

C. Motion Tests of the Untethered Robotic Millipede on Smooth Surfaces

To evaluate the performance of the whole untethered robotic millipede, we first set up a laboratory environment to test its locomotion (Supplementary Video Part 3). For the untethered motions, the robot was driven by the integrated valves and pumps on it with a lower flow rate than that generated by the pressure regular used in the tethered experiment. Therefore, the robot's performance was constrained by the pump and valve's flow rate. As shown in Fig. 9(a), we tested its forward motion tests on a flat surface with four different period durations (the driving sequences of the valves are shown in Fig. 9(b)). Results in Fig. 9(c) show that the average velocity got its maximum of 30.96 cm/min (1.35 body length per minute) with a period of 1.2 s (0.83 Hz). During the tests of the two inverted units driven by a 700-kPa air cylinder and a pressure regulator, the translational speed was up to 10 mm/s at 1.25 Hz, and 15 mm/s at 2.5 Hz. Yet the untethered robot only achieved a maximum speed of 30.96 cm/min (which is 5.2 mm/s). This difference indicates

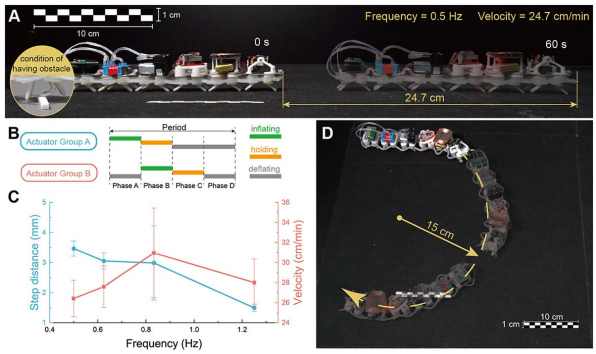

Fig. 9. Locomotion of the robotic millipede on a flat surface. (a) Snapshots of forwarding motion. (b) Drive sequence of the two groups of actuators during a cycle. (c) The robot's forward velocity with period duration. (d) Snapshot of steering motion.

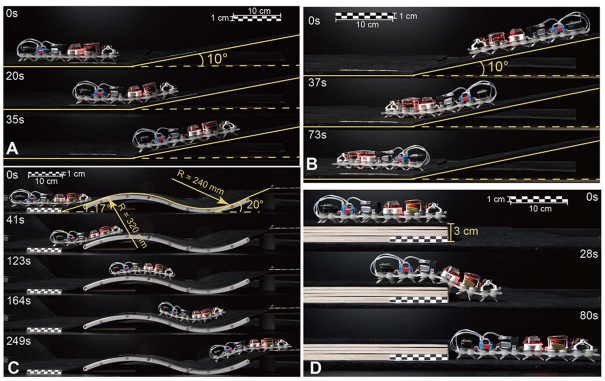

Fig. 10. Locomotion of the robotic millipede on more complex terrains. (a) Snapshots of the robot climbing from a horizontal plane to an inclined plane of 10 degrees. (b) Snapshots of the robot climbing from the 10-degree inclined plane back to the horizontal plane. (c) Snapshots of the robot moving along an undulating terrain. (d) Snapshots of the robot moving from a 3-cm-high stepped terrain to the ground.

that the flow rate and pressure of the portable pump limit the speed of the microfluidic actuators and the robot. Fig. 9(d) shows that the robot achieved a steering motion of 180 degrees with a radius of 15 cm (0.65 body length) by driving the tendons and bending the robot's active flexible joints.

Fig. 10(a) and (b) show that the robot can climb from a flat plane to an inclined plane of 10 degrees and from the 10-degree inclined plane back to the flat plane. During these processes, the flexible joints facilitate the robot's body to adapt to the sharp transition corner to ensure the ability to move [39]. Fig. 10(c) shows that the soft body of the multi-legged robot deforms to a shape that conforms well to the undulating terrain passively for efficient locomotion. The soft body also helped the robot to move from a 3cm-high stepped stair (which was three times the height of the robot's leg) to the ground with the same gait of locomotion as on a flat surface (Fig. 10(d)), which can be seen as the physical intelligence of a flexible robot [40].

D. Motion Tests of the Robotic Millipede on Uneven Terrains

Finally, we placed the robot on grass, a marble floor, and a wooden surface with gaps to characterize its locomotion performance in real-world environments (Supplementary Video Part 4). To demonstrate its potential application for search and explorations of unknown environments, we also controlled the

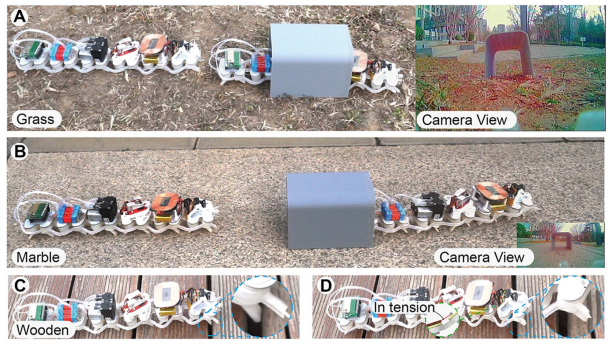

Fig. 11. Locomotion of the robotic millipede in real-world environments. (a) Snapshots of the robot moving on the grass and going across a hole and the view from the robot's equipped camera. (b) Movements on a marble floor. (c) The robot moving on wooden surfaces and stuck in a gap. (d) The robot escaping from the gap by heading up.

TABLE I
COMPARISON OF OUR ROBOTIC MILLIPEDE WITH OTHER RELATED ROBOTS WITH PNEUMATIC ACTUATORS

Related Robots	UT	BL (cm)	Aspect ratio	Weight (g)	Speed (cm/min)	L#	DS#
Drotman et al. [30]	No	N.A.	<2	N.A.	120	4	12
Tolley et al. [31]	Yes	65	<2	5000	30	4	6
Liu et al. [32]	No	23	<2	650	606	6	12
Paschal et al. [33]	Yes	23	1	N.A	36	15	8
Our robot	Yes	23	4.6	150	30.96	24	2

UT: Untethered, **BL:** Body Length, **Aspect Ratio:** Length-to-width Ratio **L#:** Number of Legs, **DS#:** Number of Independent Drive Source

robot remotely through its real-time images sent back wirelessly. Fig. 11(a) and (b) show that we successfully controlled the robot to move across a target through remote control on grass and a marble floor. In Fig. 11(c), when the robot was moving on a wooden floor with gaps, the foremost legs was stuck in a gap and the robot was trapped there. However, the robot actuated its first two joints by tightening the middle tendon and successfully took out its leg and went over the gap. Using this strategy, the robotic millipede could pass a gap of up to 2 cm in laboratory tests (Supplementary Video Part 3). This demonstration shows the robot's versatile capabilities of handling different types of terrains with both its leg and body motions.

E. Comparison of Our Robotic Millipede With Other Related Robots With Pneumatic Actuators

In Table I, we summarize some relevant legged mobile robots with pneumatic actuators and compare their key attributes with ours. As we can see from the comparison, the main advantage of our work is that it can drive 24 actuators with only two independent drive sources, which allows untethered movement with an overall light weight. Furthermore, it has small width and height to pass through narrow spaces.

V. CONCLUSION

This paper presents a millipede-inspired robot that uses a microfluidic actuator array to drive the multiple legs. This actuation method for multi-legged robots allows the system integration to

be small and weight using only two independent low-pressure sources. Even though the microfluidic actuators are soft and of low pressure, they have been demonstrated to be of sufficient displacement and load-bearing capabilities to serve as motors for the legs. In addition, the robot's soft-rigid hybrid body facilitates it to adapt actively and passively to various terrains. In the future, this small, lightweight, and flexible robotic millipede can help people explore narrow spaces and complex terrains remotely. Though promising, the locomotion speed of our untethered robotic millipede is still slow. From the comparison of the results of the actuator array units and untethered robotic millipede tests, it can be seen that the bandwidth of the actuators is limited by the small flow rate and pressure from the powering pumps. Replacing them with high-flow-rate pumps can effectively improve its locomotion performance. In addition, the robot's obstacle-overcoming capability mainly relies on its passive adaptability and open-loop control. In the future, closed-loop control can be further developed for the robot to adapt to terrain variations actively.

ACKNOWLEDGMENT

We thank Xin An, Jingyi Zhou, and Yafeng Cui for their kind assistance and suggestion throughout the project.

REFERENCES

[1] X. Wang et al., "Bioinspired footed soft robot with unidirectional all-terrain mobility," *MaterialsToday*, vol. 35, pp. 42–49, May 2020.
[2] L. Bruzzone and G. Quaglia, "Review article: Locomotion systems for ground mobile robots in unstructured environments," *Mech. Sci*., vol. 3, pp. 49–62, 2012.
[3] C. Branyan, R. L. Hatton, and Y. Mengüç, "Snake-inspired kirigami skin for lateral undulation of a soft snake robot," *IEEE Robot. Autom. Lett.*, vol. 5, no. 2, pp. 1728–1733, Apr. 2020.
[4] T. Duggan, L. Horowitz, A. Ulug, E. Baker, and K. Petersen, "Inchworm-inspired locomotion in untethered soft robots," in *Proc. IEEE 2nd Int. Conf. Soft Robot*., Seoul, Korea, 2019, pp. 200–205.
[5] C. T. Nguyen, H. Phung, P. T. Hoang, T. D. Nguyen, H. Jung, and H. R. Choi, "Development of an insect-inspired hexapod robot actuated by soft actuators," *J. Mech. Robot.*, vol. 10, no. 6, Dec. 2018, Art. no. 061016.
[6] H. Fang, Y. Zhang, and K. W. Wang, "Origami-based earthworm-like locomotion robots," *Bioinspir. Biomim.*, vol. 12, no. 6, Oct. 2017, Art. no. 065003.
[7] C. Tang et al., "A pipeline inspection robot for navigating tubular environments in the sub-centimeter scale," *Sci. Robot.*, vol. 7, no. 66, May 2022, Art. no. eabm8597.
[8] X. Dong, C. Tang, S. Jiang, Q. Shao, and H. Zhao, "Increasing the payload and terrain adaptivity of an untethered crawling robot via soft-rigid coupled linear actuators," *IEEE Robot. Autom. Lett.*, vol. 6, no. 2, pp. 2405–2412, Apr. 2021.
[9] Y. Chen et al., "Controlled flight of a microrobot powered by soft artificial muscles," *Nature*, vol. 575, no. 7782, pp. 324–329, Nov. 2019.
[10] A. Nemiroski et al., "Arthrobots," *Soft Robot.*, vol. 4, no. 3, pp. 183–190, Sep. 2017.
[11] Y. Tang et al., "Leveraging elastic instabilities for amplified performance: Spine-inspired high-speed and high-force soft robots," *Sci. Adv.*, vol. 6, no. 19, May 2020, Art. no. eaaz6912.
[12] C. T. Nguyen, H. Phung, T. D. Nguyen, H. Jung, and H. R. Choi, "Multiple-degrees-of-freedom dielectric elastomer actuators for soft printable hexapod robot," *Sens. Actuators Phys.*, vol. 267, pp. 505–516, Nov. 2017.
[13] P. E. Marek et al., "The first true millipede–1306 legs long," *Sci. Rep.*, vol. 11, Dec. 2021, Art. no. 23126.
[14] S. I. Golovatch and R. D. Kime, "Millipede (Diplopoda) distributions: A review," *Soil Org.*, vol. 81, no. 3, pp. 565–565, 2009.
[15] A. Garcia, G. Krummel, and S. Priya, "Fundamental understanding of millipede morphology and locomotion dynamics," *Bioinspir. Biomim.*, vol. 16, no. 2, Dec. 2020, Art. no. 026003.
[16] A. Torige, M. Noguchi, and N. Ishizawa, "Centipede type multi-legged walking robot," in *Proc. IEEE Int Conf. Intell. Rob. Syst.*, Yokohama, Japan, 1993, vol. 1, pp. 567–571.
[17] A. Torige, S. Yagi, H. Makino, T. Yagami, and N. Ishizawa, "Centipede type walking robot (CWR-2)," in *Proc. IEEE/RSJ Int. Conf. Intell. Robot Syst. Innov. Robot. Real-World Appl.*, 1997, vol. 1, pp. 402–407.
[18] D. Koh, J. Yang, and S. Kim, "Centipede robot for uneven terrain exploration: Design and experiment of the flexible biomimetic robot mechanism," in *Proc. IEEE RAS EMBS Int. Conf. Biomed. Rob. Biomechatron., BioRob*, Tokyo, Japan, 2010, pp. 877–881.
[19] M. Masuda and K. Ito, "Semi-autonomous centipede-like robot with flexible legs," in *Proc. IEEE Int. Symp. Saf., Secur. Rescue Robot.,* Hokkaido, Japan, 2014, pp. 1–6.
[20] K. Ito and S. Kashiwada, "Proposal of semiautonomous centipede-like robot for rubbles," *Artif. Life Robot.*, vol. 19, no. 4, pp. 400–405, Dec. 2014.
[21] Y. Ozkan-Aydin and D. I. Goldman, "Self-reconfigurable multilegged robot swarms collectively accomplish challenging terradynamic tasks," *Sci. Robot.*, vol. 6, no. 56, Jul. 2021, Art. no. eabf1628.
[22] K. L. Hoffman and R. J. Wood, "Turning gaits and optimal undulatory gaits for a modular centipede-inspired millirobot," in *Proc. IEEE RAS EMBS Int. Conf. Biomed. Rob. Biomechatron.*, Rome, Italy, 2012, pp. 1052–1059.
[23] K. L. Hoffman and R. J. Wood, "Robustness of centipede-inspired millirobot locomotion to leg failures," in *Proc. IEEE Int. Conf. Intell. Rob. Syst.*, Tokyo, 2013, pp. 1472–1479.
[24] H. Lu et al., "A bioinspired multilegged soft millirobot that functions in both dry and wet conditions," *Nat. Commun.*, vol. 9, no. 1, Dec. 2018, Art. no. 3944.
[25] H. Gu et al., "Magnetic cilia carpets with programmable metachronal waves," *Nat. Commun.*, vol. 11, no. 1, Dec. 2020, Art. no. 2637.
[26] H. Lu, Y. Hong, Y. Yang, Z. Yang, and Y. Shen, "Battery-less soft millirobot that can move, sense, and communicate remotely by coupling the magnetic and piezoelectric effects," *Adv. Sci.*, vol. 7, no. 13, Jul. 2020, Art. no. 2000069.
[27] R. Tan et al., "Nanofiber-based biodegradable millirobot with controllable anchoring and adaptive stepwise release functions," *Matter*, vol. 5, no. 4, pp. 1277–1295, Apr. 2022.
[28] A. D. Marchese, C. D. Onal, and D. Rus, "Autonomous soft robotic fish capable of escape maneuvers using fluidic elastomer actuators," *Soft Robot.*, vol. 1, no. 1, pp. 75–87, Mar. 2014.
[29] R. F. Shepherd et al., "Multigait soft robot," *Proc. Nat. Acad. Sci.*, vol. 108, no. 51, pp. 20400–20403, Dec. 2011.
[30] D. Drotman, S. Jadhav, M. Karimi, P. de Zonia, and M. T. Tolley, "3D printed soft actuators for a legged robot capable of navigating unstructured terrain," in *Proc. IEEE Int. Conf. Robot. Autom.*, Singapore, 2017, pp. 5532–5538.
[31] M. T. Tolley et al., "A resilient, untethered soft robot," *Soft Robot.*, vol. 1, no. 3, pp. 213–223, Sep. 2014.
[32] Z. Liu, Z. Lu, and K. Karydis, "SoRX: A soft pneumatic hexapedal robot to traverse rough, steep, and unstable terrain," in *Proc. IEEE Int. Conf. Robot. Autom*., 2020, pp. 420–426.
[33] T. Paschal, M. A. Bell, J. Sperry, S. Sieniewicz, R. J. Wood, and J. C. Weaver, "Design, fabrication, and characterization of an untethered amphibious sea urchin-inspired robot," *IEEE Robot. Autom. Lett.*, vol. 4, no. 4, pp. 3348–3354, Oct. 2019.
[34] K. P. Becker, Y. Chen, and R. J. Wood, "Mechanically programmable dip molding of high aspect ratio soft actuator arrays," *Adv. Funct. Mater.*, vol. 30, no. 12, 2020, Art. no. 1908919.
[35] P. Polygerinos et al., "Soft robotics: Review of fluid-driven intrinsically soft devices; manufacturing, sensing, control, and applications in human-robot interaction," *Adv. Eng. Mater.*, vol. 19, no. 12, 2017, Art. no. 1700016.
[36] D. Avirovik, B. Butenhoff, and S. Priya, "Millipede-inspired locomotion through novel u-shaped piezoelectric motors," *Smart Mater. Struct.*, vol. 23, no. 3, 2014, Art. no. 037001.
[37] H. O. Foster, "Inflation of a plane circular membrane," *J. Eng. Ind.*, vol. 89, no. 3, pp. 403–407, Aug. 1967.
[38] L. Marechal, P. Balland, L. Lindenroth, F. Petrou, C. Kontovounisios, and F. Bello, "Toward a common framework and database of materials for soft robotics," *Soft Robot*., 8, no. 3, pp. 284–297, Jun. 2020.
[39] W. Haomachai, D. Shao, W. Wang, A. Ji, Z. Dai, and P. Manoonpong, "Lateral undulation of the bendable body of a gecko-inspired robot for energy-efficient inclined surface climbing," *IEEE Robot. Autom. Lett.*, vol. 6, no. 4, pp. 7917–7924, Oct. 2021.
[40] M. Sitti, "Physical intelligence as a new paradigm," *Extreme Mech. Lett.*, vol. 46, Jul. 2021, Art. no. 101340.